



# Benchmarking the accuracy of higher order particle methods in geodynamic models of transient flow

Rene Gassmöller<sup>1</sup>, Juliane Dannberg<sup>1</sup>, Wolfgang Bangerth<sup>2</sup>, Elbridge Gerry Puckett<sup>3</sup>, and Cedric Thieulot<sup>4</sup>

<sup>1</sup>Department of Geological Sciences, University of Florida

<sup>2</sup>Department of Mathematics, Colorado State University

<sup>3</sup>Department of Mathematics, University of California, Davis

<sup>4</sup>Department of Earth Sciences, Utrecht University

**Correspondence:** Rene Gassmöller (rene.gassmoeller@ufl.edu)

**Abstract.** Numerical models are a powerful tool for investigating the dynamic processes in the interior of the Earth and other planets, but the reliability and predictive power of these discretized models depends on the numerical method, as well as an accurate representation of material properties in space and time. In the specific context of geodynamic models, particle methods have been applied extensively because of their suitability for advection-dominated processes, and have been used in applications such as tracking the composition of solid rock and melt in the Earth's mantle, fluids in lithospheric- and crustal-scale models, light elements in the liquid core, and deformation properties like accumulated finite strain or mineral grain size, along with many applications outside the Earth sciences.

There have been significant benchmarking efforts to measure the accuracy and convergence behavior of particle methods, but these efforts have largely been limited to instantaneous solutions, or time-dependent models without analytical solutions. As a consequence, there is little understanding about the interplay of particle advection errors and errors introduced in the solution of the underlying transient, nonlinear flow equations. To address these limitations, we present two new dynamic benchmarks for transient Stokes flow with analytical solutions that allow us to quantify the accuracy of various advection methods in nonlinear flow. We use these benchmarks to measure the accuracy of our particle algorithm as implemented in the ASPECT geodynamic modeling software against commonly employed field methods and analytical solutions. In particular, we quantify if an algorithm that is higher-order accurate in time will allow for better overall model accuracy and verify that our algorithm reaches its intended optimal convergence rate. We then document that the observed increased accuracy of higher-order algorithms matters for geodynamic applications with an example of modeling small-scale convection underneath an oceanic plate and show that the predicted place and time of onset of small-scale convection depends significantly on the chosen particle advection method.

Descriptions and implementations of our benchmarks are openly available and can be used to verify other advection algorithms. The availability of accurate, scalable and efficient particle methods as part of the widely used open source code ASPECT will allow geodynamicists to accurately investigate more complex time-dependent geodynamic processes, such as elastic deformation, anisotropic fabric development, melt generation and migration, and grain damage.



## 1 Introduction

25 Numerical models have been a key tool for geoscientists investigating the processes governing plate tectonics and mantle convection. Among the many one could cite, a cross-section of publications include studies of the evolution of mantle heterogeneities over time (Gülcher et al., 2021; Jones et al., 2021), the initiation and evolution of plate boundaries (Baes et al., 2020; Schierjott et al., 2020), the fate of subducted slabs (Grima et al., 2020), plume dynamics (Arnould et al., 2020), the dynamics of microplates (Glerum et al., 2020), and the seismic cycle (Van Zelst et al., 2019). Obviously, the usefulness of such dynamic  
30 models relies on the accurate approximation of solutions of the equations that describe the processes under consideration. For geodynamic models of the solid Earth, this usually requires solving the Stokes equations governing the flow, and advection(-diffusion) equations governing the transport of thermodynamic properties like temperature or entropy, chemical composition, trace elements, deformation properties like damage, or mineralogical properties like grain size. Established methods for solving the Stokes equations typically treat the fluid as a continuum and are based on the finite-element, finite-difference, and  
35 finite-volume methods. In contrast, there is a wide variety of methods for solving the advection equations (Puckett et al., 2018), such as particle methods, continuous or discontinuous field methods, or volume-of-fluid methods.

Over the past years we have developed a flexible, scalable, and efficient particle architecture (Gassmüller et al., 2018) as part of our work developing the Advanced Solver for Planetary Evolution, Convection, and Tectonics (ASPECT, Kronbichler et al., 2012; Heister et al., 2017). This work is open-source, application agnostic, and performs well in modern high-performance  
40 computing environments. In particular, it supports advanced computational methods such as an adaptively refined, unstructured, and dynamically changing background mesh, parallelization beyond tens of thousand of compute cores, storing arbitrary particle properties, and complex nonlinear solvers. The underlying particle infrastructure is integrated into the open source finite element software library deal.II (Arndt et al., 2023) and has been used to model geoscientific applications, as well as Navier-Stokes flow, mixing of granular materials, solid-fluid interaction, and laser metal deposition of metallic particles (Popov and  
45 Marchevsky, 2022; Arndt et al., 2020; Golshan et al., 2022; El Geitani et al., 2023; Golshan and Blais, 2022; Murer et al., 2022).

Due to their inherent suitability for modeling advection-dominated problems, different variants of particle methods have become popular in the geodynamic modeling community (van Keken et al., 1997; Tackley and King, 2003; Gerya and Yuen, 2003; Samuel, 2018; Sime et al., 2021). The main advantage of particles in geodynamic applications is that particles advected  
50 with the material flow keep their associated material properties; that is, these properties do not diffuse in space as is the case for many field-based methods. It also means that the differential equations for each particle's location are simply ordinary differential equations for which many good solution approaches are available. On the other hand, while errors in particle methods are less apparent than for field methods, they still exist (Tackley and King, 2003; Gassmüller et al., 2019). In particular, previous work has discussed the influence of errors due to interpolating properties from particles to fields (Thielmann et al.,  
55 2014), the influence of the divergence of the computed velocity field on particle distributions (Wang et al., 2015; Pusok et al., 2017; Sime et al., 2021), and the advection of particles over time in spatially variable flow (Gassmüller et al., 2019). However, a source of error in particle advection methods that has, to the best of our knowledge, not been systematically discussed is the



error in advecting the particle position in transient, rapidly changing flow. This type of flow is common in geodynamic models of the upper mantle or lithosphere, because employing a visco-plastic or stress-dependent rheology can cause strong nonlinear feedbacks between the current solution and material properties and therefore fast changes over time. While the presence of these errors is known, only few studies systematically investigate its influence on geodynamic applications (Trim et al., 2023a, b). This is largely due to the difficulty of quantifying their influence, as one needs a time-dependent model solution to compare numerical results against, and most currently available benchmarks either rely on instantaneous solutions (Duretz et al., 2011; Zhong, 1996; Zhong et al., 2008; Schmid and Podladchikov, 2003; Kramer et al., 2021), a steady-state solution (Zhong et al., 2008; Gassmüller et al., 2019) or a comparison between several numerical methods without known exact solution (Tackley and King, 2003; van Keken et al., 1997).

In this work, we start with a description of the mathematical problem we would like to solve in Section 2, and then present an analysis of the numerical errors that result from the advection of particles in transient flow (Section 3). We develop new benchmarks for transient flow in a box and spherical shell that have known analytical solutions (Section 4), and use these benchmarks to measure the accuracy of the discussed particle advection methods and quantify their influence on the results of the Stokes equations (Section 5). Finally, we illustrate why focusing on the accuracy of particle methods matters for practical geodynamic applications with a model example of small-scale convection developing underneath oceanic lithosphere (Section 6). We conclude in Section 7. Appendix A contains the derivation of the analytical solution for the spherical shell benchmark, and Appendix B contains a more detailed discussion of some benchmark results that are too specific to be relevant for the main text.

## 2 Governing equations

For the models in this work, we will consider the incompressible Stokes equations using the Boussinesq approximation. They consist of a force balance and a mass continuity equation:

$$-\nabla \cdot (2\eta \dot{\epsilon}(\mathbf{u})) + \nabla p = \rho \mathbf{g}, \quad (1)$$

$$\nabla \cdot \mathbf{u} = 0, \quad (2)$$

where  $\mathbf{u} = \mathbf{u}(\mathbf{x}, t)$  is the velocity,  $p = p(\mathbf{x}, t)$  the pressure,  $\rho$  the density,  $\eta$  the viscosity, and  $\mathbf{g}$  the gravity.  $\dot{\epsilon}(\mathbf{u}) = \frac{1}{2}(\nabla \mathbf{u} + \nabla \mathbf{u}^T)$  denotes the strain rate. The velocity and pressure variables depend on time because the density and viscosity may depend on time through the variables we describe below; in other words, because inertia is absent the equations above describe a time-dependent but instantaneous equilibrium.

To determine the time evolution of the model, we solve advection-diffusion equations of the form

$$\frac{D\phi_c}{Dt} - \nabla \cdot (\kappa_c \nabla \phi_c) = \frac{\partial \phi_c}{\partial t} + \mathbf{u} \cdot \nabla \phi_c - \nabla \cdot (\kappa_c \nabla \phi_c) = H_c, \quad (3)$$

where  $\phi_c = \phi_c(\mathbf{x}, t)$  denotes an advected material property,  $\kappa_c$  its diffusivity, and  $H_c$  additional source terms. The subscript  $c = 1, \dots, N_c$  indicates that practical applications may require several advected material properties.



Throughout this paper we focus on problems with negligible diffusion ( $\kappa_c = 0$ ), which represent for example the advection  
90 of the chemical composition of rocks, or the size of grains; particle methods for applications with non-negligible diffusivity  
and reactions have been described elsewhere (Gerya and Yuen, 2003; Sime et al., 2022). Consequently, instead of equation (3)  
we will solve:

$$\frac{\partial \phi_c}{\partial t} + \mathbf{u} \cdot \nabla \phi_c = H_c. \quad (4)$$

In Equations (1), (2), and (4), material properties  $\eta$ ,  $\rho$  and source terms  $H_c$  may depend non-linearly on the solution variables  
95  $\mathbf{u}$ ,  $p$ , and  $\phi_c$ , resulting in a coupled system of equations.

While for simplicity we use the incompressible Stokes equations, the usefulness of the benchmark models we present below  
do not rely on this assumption and will be transferable to compressible models. In fact, an accurate solution to the advection  
equation may matter more in compressible models, because they often contain more coupled terms, such as shear heating  
(depending on the strain rate), the pressure dependence of the density, and additional processes like phase transitions caused  
100 by pressure or temperature changes.

### 3 Numerical methodology

We have discussed the numerical methods for most steps of our particle algorithm (Gassmüller et al., 2018, 2019) and Stokes  
solver (Kronbichler et al., 2012; Heister et al., 2017) in earlier work and refer there for details on the finite-element method,  
time stepping algorithm, particle generation, advection, and interpolation from particles to grid. Here we will extend this  
105 earlier work by developing transient solutions, and focus on how the temporal accuracy of advection methods controls the  
overall accuracy of a coupled geodynamic model.

#### 3.1 Particle advection

In particle methods, the values of fields  $\phi_c$  are approximated by advecting particles that carry these field value as “properties”.  
Particles move with the velocity  $\mathbf{u}(\mathbf{x}, t)$  that results from solving the Stokes equations (1)–(2), and the properties carried by  
110 a particle evolve based on the right hand side  $H_c$  in (4). In other words, the solution of the partial differential equation (4) is  
approximated by solving an ordinary differential equation (ODE) tracking the position  $\mathbf{x}_j = \mathbf{x}_j(t)$  for each particle  $j$ , and a  
separate ODE tracking the evolution of the properties carried by the particle:

$$\frac{d}{dt} \mathbf{x}_j(t) = \mathbf{u}(\mathbf{x}_j(t), t), \quad (5)$$

$$\frac{d}{dt} \phi_{c,j}(t) = H_c(\mathbf{x}_j(t), t, \phi_{c,j}(t)). \quad (6)$$

115 In practice, the exact velocity  $\mathbf{u}(\mathbf{x}, t)$  is not available, but only a numerical approximation in space  $\mathbf{u}_h(\mathbf{x}, t)$  to  $\mathbf{u}(\mathbf{x}, t)$ .  
Furthermore, this approximation is only available at discrete time steps,  $\mathbf{u}_h^n(\mathbf{x}) = \mathbf{u}_h(\mathbf{x}, t^n)$  and it needs to be interpolated  
between time steps if the advection algorithm for integrating (5) requires one or more evaluations at intermediate times between



$t^n$  and  $t^{n+1}$ . If we denote this interpolation in time by  $\tilde{\mathbf{u}}_h(\mathbf{x}, t)$  where  $\tilde{\mathbf{u}}_h(\mathbf{x}, t^n) = \mathbf{u}_h^n(\mathbf{x})$ , then the equation the differential equation solver really tries to solve is

$$120 \quad \frac{d}{dt} \tilde{\mathbf{x}}_j(t) = \tilde{\mathbf{u}}_h(\mathbf{x}_j(t), t), \quad (7)$$

where  $\tilde{\mathbf{x}}_j(t)$  is the exact solution of this equation using the “wrong” velocity field; if  $\tilde{\mathbf{u}}_h$  is a good approximation to  $\mathbf{u}$ , then we hope that  $\tilde{\mathbf{x}}(t)$  is a good approximation of  $\mathbf{x}(t)$ . In practice, however, we can not even compute  $\tilde{\mathbf{x}}(t)$ , but need to further approximate it via time stepping.

### 3.2 Convergence of particle advection methods

125 The total error in computed particle positions contains contributions due to the inexactly known velocity field discussed in the previous subsection, as well as the error introduced by time stepping the ODEs describing particle position and properties. If we denote by  $\tilde{\mathbf{x}}_{j,h}(t)$  the numerical approximation to the solution of (7), then the error at some time  $t$  will typically satisfy a relationship like

$$\|\tilde{\mathbf{x}}_{j,h}(t) - \tilde{\mathbf{x}}_j(t)\| \leq C(t)\Delta t_p^q, \quad (8)$$

130 where  $\Delta t_p$  is the time step used by the ODE solver, which is often an integer fraction of the time step  $\Delta t_u$  used to advance the velocity field  $\mathbf{u}$ . In our application we will choose  $\Delta t_p = \Delta t_u$ .  $q$  is the convergence order of the method, and  $C(t)$  is a (generally unknown) constant that depends on the end time  $t$  at which one compares the solutions as well as on  $\tilde{\mathbf{u}}$ . We want to compare this computed solution against “exact” trajectories using the *exact* velocity as in (5), and then assess the error as  $\|\mathbf{x}_j(t) - \tilde{\mathbf{x}}_{j,h}(t)\|$ . This quantity will, in the best case, only satisfy an estimate of the form

$$135 \quad \begin{aligned} \|\tilde{\mathbf{x}}_{j,h}(t) - \mathbf{x}_j(t)\| &= \|(\tilde{\mathbf{x}}_{j,h}(t) - \tilde{\mathbf{x}}_j(t)) + (\tilde{\mathbf{x}}_j(t) - \mathbf{x}_j(t))\| \\ &\leq \|\tilde{\mathbf{x}}_{j,h}(t) - \tilde{\mathbf{x}}_j(t)\| + \|\tilde{\mathbf{x}}_j(t) - \mathbf{x}_j(t)\| \\ &\leq C_1(t)\Delta t_p^q + C_2(t)\|\mathbf{u} - \mathbf{u}_h\| + C_3(t)\|\mathbf{u}_h - \tilde{\mathbf{u}}_h\|, \end{aligned}$$

with appropriately chosen norms for the second and third term, which represent how accurately the flow field itself is discretized in space and time. All of these terms can converge to zero at different rates with the mesh size  $h$  and the time step size  $\Delta t$ ; as  
 140 a consequence, each of these terms may be the limiting factor for the overall accuracy of the ODE integrator.

### 3.3 Common particle integrators

Given these considerations, and given that ODE integrators require the expensive step of evaluating the velocity field  $\tilde{\mathbf{u}}_h$  at arbitrary points in time and space, choosing a simpler, less accurate scheme can significantly reduce the computation time. In our work, we have implemented the Forward Euler, Runge–Kutta 2 (RK2) and Runge–Kutta 4 (RK4) schemes (Hairer  
 145 and Wanner, 1991; Gassmüller et al., 2018), although many other methods are available and have been used in geodynamic applications. We will briefly discuss our selected methods below and will then limit ourselves to a discussion of two different variants of the RK2 integrator, which is sufficient to support our conclusions.



For simplicity, we will omit the particle index  $j$  from formulas in the remainder of this section and will assume that the ODE and PDE time steps  $\Delta t_p, \Delta t_u$  are equal. We will therefore simply denote them as  $\Delta t$ . This is often the case in practice because the velocity field is typically computed with a method that requires a Courant-Friedrichs-Lewy (CFL) number around or smaller than one, implying that particles move no more than by one cell diameter per (PDE) time step. In such cases, even explicit time integrators for particle trajectories can be used without leading to instabilities, and all of the methods below fall in this category. The formulas in the remainder of this section are, however, obvious to generalize to cases where  $\Delta t_p < \Delta t_u$ . We will also assume in the following that we have already solved the velocity field up to time  $t^{n+1}$  and are now updating particle locations from  $\mathbf{x}^n$  to  $\mathbf{x}^{n+1}$ . In cases where one wants to solve for particle locations *before* updating the velocity field,  $\tilde{\mathbf{u}}_h$  can be extrapolated beyond  $t^n$  from previous time steps, or particle advection and velocity computation could be iterated in a nonlinear solver scheme.

In the following, let us briefly describe some of the common time stepping algorithms, including those we use in this work.

1. Forward Euler (FE): The simplest method often used is the forward Euler scheme,

$$\tilde{\mathbf{x}}^{n+1} = \tilde{\mathbf{x}}^n + \Delta t \tilde{\mathbf{u}}_h(t^n, \tilde{\mathbf{x}}^n).$$

It is only of first order (that is, the exponent in (8) is  $q = 1$ ), but cheap to evaluate because it only requires evaluating the velocity solution at an already-computed time point.

2. Runge–Kutta second order (RK2): Accuracy and stability can be improved by using a second order Runge–Kutta scheme. The new particle position is computed as

$$\mathbf{k}_1 = \frac{\Delta t}{2} \tilde{\mathbf{u}}_h(t^n, \tilde{\mathbf{x}}^n),$$

$$\tilde{\mathbf{x}}^{n+1} = \tilde{\mathbf{x}}^n + \Delta t \tilde{\mathbf{u}}_h\left(t^n + \frac{\Delta t}{2}, \tilde{\mathbf{x}}^n + \frac{\mathbf{k}_1}{2}\right).$$

This method is second order (that is,  $q = 2$  in (8)) but requires evaluating the computed velocity at a time point intermediate between (velocity) time steps.

3. Runge–Kutta second-order space, first-order time (RK2FOT): In practice many geodynamic modeling packages only store a single velocity solution at a time, which prevents the interpolation of the velocity field at  $t^n + \frac{\Delta t}{2}$  used in RK2 from adjacent solutions at  $t^n$  and  $t^{n+1}$ . However, reasonable accuracy can still often be achieved when ignoring the time dependence of the velocity (Gerya and Yuen, 2003; McNamara and Zhong, 2004). We here implement such an advection scheme as a modification to RK2, in which the new particle position is computed as

$$\mathbf{k}_1 = \frac{\Delta t}{2} \tilde{\mathbf{u}}_h(t^n, \tilde{\mathbf{x}}^n),$$

$$\tilde{\mathbf{x}}^{n+1} = \tilde{\mathbf{x}}^n + \Delta t \tilde{\mathbf{u}}_h\left(t^n, \tilde{\mathbf{x}}^n + \frac{\mathbf{k}_1}{2}\right).$$

Note how, compared to the RK2 scheme, the velocity is evaluated at  $t^n$  instead of  $t^n + \frac{\Delta t}{2}$ .



4. Runge–Kutta fourth order (RK4): A further improvement of particle advection can be achieved by a fourth order Runge–Kutta scheme that computes the new position as

$$\begin{aligned} \mathbf{k}_1 &= \Delta t \tilde{\mathbf{u}}_h(t^n, \tilde{\mathbf{x}}^n), \\ \mathbf{k}_2 &= \frac{\Delta t}{2} \tilde{\mathbf{u}}_h\left(t^n + \frac{\Delta t}{2}, \tilde{\mathbf{x}}^n + \frac{\mathbf{k}_1}{2}\right), \\ \mathbf{k}_3 &= \frac{\Delta t}{2} \tilde{\mathbf{u}}_h\left(t^n + \frac{\Delta t}{2}, \tilde{\mathbf{x}}^n + \frac{\mathbf{k}_2}{2}\right), \\ \mathbf{k}_4 &= \Delta t \tilde{\mathbf{u}}_h(t^{n+1}, \tilde{\mathbf{x}}^n + \mathbf{k}_3), \\ \tilde{\mathbf{x}}^{n+1} &= \tilde{\mathbf{x}}^n + \frac{1}{6}\mathbf{k}_1 + \frac{1}{3}\mathbf{k}_2 + \frac{1}{3}\mathbf{k}_3 + \frac{1}{6}\mathbf{k}_4. \end{aligned}$$

The primary expense in all of the methods above is the evaluation of the velocity field  $\mathbf{u}_h^n$  and  $\mathbf{u}_h^{n+1}$  at arbitrary positions  $\mathbf{x}$ . Given that the velocity fields  $\mathbf{u}_h$  we consider here are often finite element fields defined with shape functions whose values are determined by mapping a reference cell  $\hat{K}$  to each cell  $K$  using a transformation  $\mathbf{x} = \Phi_K(\hat{\mathbf{x}})$ , the evaluation at arbitrary points requires the inversion of  $\Phi_K$ , which is an expensive operation for nonlinear mappings such as those used in deformed or curved geometries.

### 3.4 Particle integrators used in the benchmarks

Based on our earlier work measuring the convergence properties of the integrators described above in analytically known flow (Gassmüller et al., 2018, supp. information) we expect FE and RK2FOT to converge with first order (in  $\Delta t$ ) in time variable flow, while RK2 and RK4 are expected to converge with second order in time. RK2FOT is limited from reaching the potential of RK2 by the use of only a single velocity solution in time, and RK4 in our specific implementation (though not in general) is limited by only storing two velocity solutions, which only allows for a linear extrapolation from  $t^n$  to  $t^n + \frac{\Delta t}{2}$  and  $t^{n+1}$ . Therefore, while there are valid reasons to choose either FE or RK4, we will limit our benchmark results to RK2 and RK2FOT, because we expect them to illustrate the significant difference between algorithms that are first- or second-order accurate in time.

## 4 Deriving transient benchmark solutions

For our benchmarks we want to reduce the coupling between (1)–(2) and (4) to a minimum in order to precisely measure the influence of exactly one coupled property. This step also simplifies the construction of the benchmarks. Therefore, we focus on problems with constant viscosity ( $\eta = 1$ ), and no source terms ( $H_c = 0$ ). The advected material property  $\phi_c$  we consider here



is the density  $\rho$ . The final set of equations for our benchmarks will therefore be:

$$-\nabla \cdot (2\dot{\epsilon}(\mathbf{u})) + \nabla p = \rho \mathbf{g}, \quad (9)$$

$$\nabla \cdot \mathbf{u} = 0, \quad (10)$$

205  $\frac{\partial \rho}{\partial t} + \mathbf{u} \cdot \nabla \rho = 0. \quad (11)$

The set of benchmarks we will consider is an extension of previously published benchmarks (Gassmüller et al., 2019). In order to explain the extensions to transient flow, we will here briefly revisit our approach to derive steady flow fields. In our earlier work we have considered incompressible flow fields  $\mathbf{u}$  that were derived based on a known and time-independent stream function  $\Psi$ . Under the assumption that viscosity is known and constant, and that boundary conditions are chosen to match the desired solution, this allowed us to compute right-hand side terms to Equation (9) that satisfied the set of equations and therefore created an analytical benchmark for the whole system of equations. However, this only guarantees a consistent solution for the distribution of the density  $\rho$  at the current instant in time. It is therefore only an *instantaneous* benchmark solution. In order to create a steady-state flow field — defined as a velocity field  $\mathbf{u}$  that does not change over time — the right-hand side driving force needs to stay constant over time. In other words the advected property  $\rho$  needs to be chosen in such a way that when it is advected with the flow field  $\mathbf{u}$ , the right-hand side  $\rho \mathbf{g}$  does not change over time. In order to find such a density distribution, we can make use of the definition of the streamline, which are lines of constant  $\Psi$ . If  $\Psi$  is independent of time, any property advected with the flow will be advected along the streamlines. Thus, if  $\rho$  is constant along the streamlines, the right-hand-side  $\rho \mathbf{g}$  will not change even if  $\rho$  is advected with the flow. Choosing  $\rho = \Psi$  is therefore an easy approach to guarantee a steady-state flow field.

220 The benchmarks below extend these steady-state models with a nonlinear time-dependence, which will test how much error the chosen advection scheme accumulates over time when the velocity changes. In order to derive such solutions, we make use of the fact that we can superimpose two independent flow fields. In addition to a steady flow based on a stream function  $\Psi$  we add a time-dependent velocity that has two special properties: First, we ensure that this second flow field is purely forced by the boundary conditions instead of internal density forces. This choice opens up control over the exact velocity over time. It also implies that we do not have to modify the density distribution to add this second flow field, i.e., the density is still a function of the steady-state stream function  $\Psi$ . Second, we will choose the time-variable flow field to be in the nullspace of the Stokes operator, e.g., solid-body rotational flow in a spherical shell and translational flow in a box geometry. This ensures that the resulting modification only affects the velocity solution (but not the pressure), and can be interpreted as a (time-dependent) coordinate transformation of a steady flow. We will consider one case in a two-dimensional spherical shell, and one case in a two-dimensional box geometry and will discuss the specific flow fields in the following subsections.

#### 4.1 A benchmark for a 2D spherical shell

Extending our previously published spherical benchmark (Gassmüller et al., 2019) seems to be straightforward by adding a time-dependent solid body rotation to the existing solution. However, because our earlier solution is already a purely rotational flow an additional time-dependent rotation does not create a transient solution for the density, and thus does not allow to



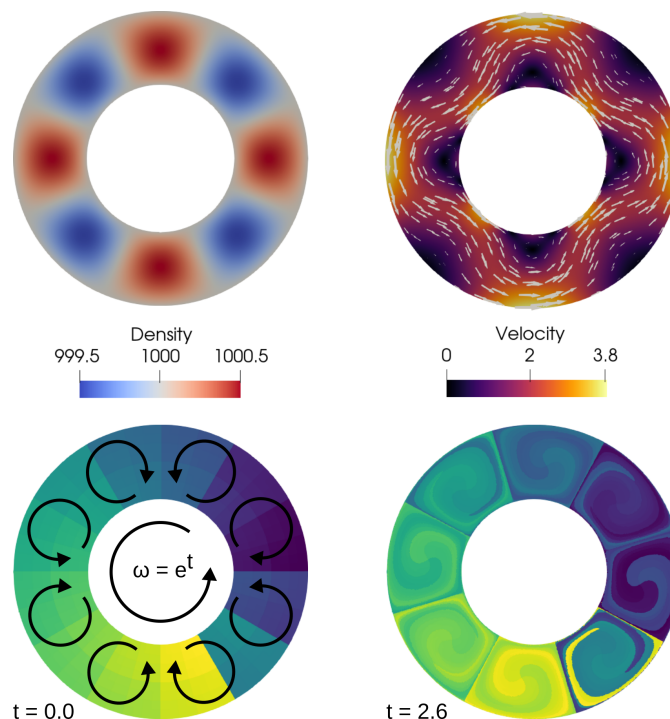


**Figure 1.** Solution of a transient spherical shell benchmark. Top left: The density field of the benchmark at  $t = 0$ . Top right: Velocity solution at  $t = 0$ . Bottom row: Initial ( $t = 0$ ) and later ( $t = 2.6$ ) particle distributions after almost two full rotations of the model. Particles are colored based on a unique index given to each particle at the beginning.

235 intuitively measure the accuracy of the combined particle-finite-element algorithm. In other words an error of the particle position along the streamline because of the time-variability of the flow would not change the density distribution and therefore would not translate into an error in the Stokes solution. We therefore use a different approach whose detailed derivation is given in Appendix A. It is important to note that while the benchmark is derived in polar coordinates, it is implemented in Cartesian coordinates in our code.



240 As described, we start from an instantaneous solution for Stokes flow in a spherical shell and add a time-dependent rotational flow that is enforced using the boundary conditions. Our final benchmark solution is

$$v_r(r, \theta, t) = g(r)k \sin(k(\theta - \tau(t))), \quad (12)$$

$$v_\theta(r, \theta, t) = f(r) \cos(k(\theta - \tau(t))) + r\omega(t), \quad (13)$$

$$p(r, \theta, t) = kh(r) \sin(k(\theta - \tau(t))), \quad (14)$$

$$245 \quad \rho(r, \theta, t) = - \left( \frac{A}{2} r^2 + B \ln(r) - 1 \right) \cos(k(\theta - \tau(t))), \quad (15)$$

$$g_r(r, \theta, t) = m(r)k \frac{\sin(k(\theta - \tau(t)))}{\rho(r, \theta, t)}, \quad (16)$$

$$g_\theta = 0. \quad (17)$$

The constants  $A, B$  and functions  $g(r), f(r), h(r), m(r)$  are listed in the appendix. The parameter  $k$  controls the number of upwellings and downwellings in the model and is chosen as  $k = 4$  for this study. The parameter  $\omega(t)$  represents the time-  
 250 dependent solid body rotation and is chosen as  $\omega(t) = e^t$ .  $\tau(t)$  is a phase shift caused by the solid body rotation, and is computed as  $\tau(t) = \int_0^t \omega(s) ds$ . The setup of the benchmark and a snapshot of the solution is shown in Fig. 1.

We note that this solution can be interpreted as consistent with a stream function that is variable in time, with a flow field that conveniently advects the density in such a way as to satisfy our Stokes solution at the current point in time. We also note that this solution effectively consists of two parts, a density-driven internal convection in small convection cells, and a forced  
 255 and analytically known rotational flow of the whole model.

## 4.2 A benchmark for a 2D box geometry

The modification to the solution of the box benchmark of (Gassmüller et al., 2018) is analogous to the spherical shell case, but we can build directly on our earlier model setup. We can add a solid body translation to our earlier solution, and with proper periodic boundary conditions this allows us to define a known, transient solution to the incompressible Stokes equations.  
 260 The translation of the solution as well as the periodic boundary conditions also represent the main difference between our benchmark solution and the one presented in (Trim et al., 2023a), which uses a steady-state flow with a time-dependent velocity amplitude.

As in the spherical case, we start by modifying the velocity in the  $x$ -direction to

$$v_x(x, y, t) = v_x(x - \tau(t), y) + \omega(t). \quad (18)$$

265 Since the solid body translation  $\omega$  is in the nullspace of the Stokes equation, it does not modify the solution except for a coordinate transformation  $x \rightarrow x - \tau(t)$  by a phase shift  $\tau(t)$ ,

$$\tau(t) = \int_0^t \omega(s) ds. \quad (19)$$

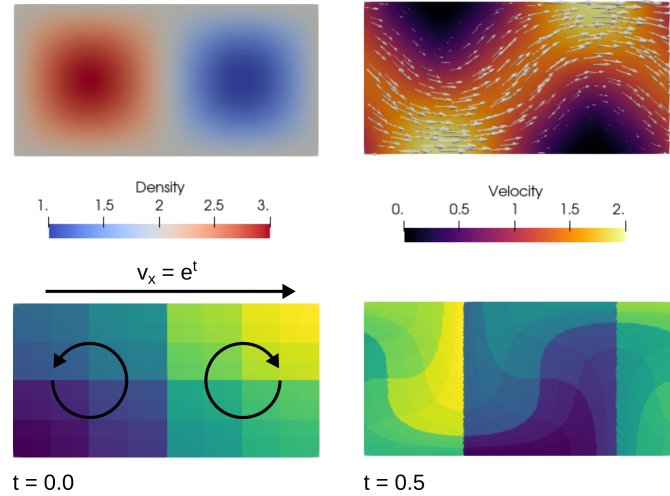


**Figure 2.** Solution of a transient box benchmark with known analytic solution. Top left: The density field of the benchmark. Top right: Velocity solution. Bottom row: Particle distributions at model start ( $t = 0$ ) and at  $t = 0.5$ . Particles are colored as in Fig. 1.

As for the spherical case described above, we will use a nonlinear choice for  $\omega(t)$ , namely  $\omega(t) = e^t$ , and the phase shift  $\tau$  is computed as before.

270 Thus, the transient solution of the benchmark – shown in Fig. 2 – is:

$$v_x(x, y, t) = \sin(\pi(x - \tau(t)) \cos(\pi y) + \omega(t), \quad (20)$$

$$v_y(x, y, t) = -\cos(\pi(x - \tau(t)) \sin(\pi y), \quad (21)$$

$$p(x, y, t) = 2\pi \cos(\pi(x - \tau(t)) \cos(\pi y), \quad (22)$$

$$\rho(x, y, t) = \sin(\pi(x - \tau(t)) \sin(\pi y), \quad (23)$$

275  $g_x(x, y, t) = 0, \quad (24)$

$$g_y(x, y, t) = -4\pi^2 \frac{\cos(\pi(x - \tau(t)) \sin(\pi y)}{\rho(x, y, t)}. \quad (25)$$

### 4.3 How we use these benchmarks in our particle advection algorithms

Adding time dependence to the benchmarks modifies the numerical solution and the accumulated error in distinct ways, depending on which advection method we choose. Here we will consider five cases:

- 280 (1) We obtain a computed solution by using the exact density  $\rho(x, y, t)$  defined in (15) and (23). This solution will act as our baseline benchmark, illustrating the optimal convergence rate for the Stokes solver we used.
- (2) We use the (interpolated) exact density as an initial condition for the density advection equation (11), whose solution we then approximate using discontinuous, piecewise quadratic ( $DGQ_2$ ) finite elements with a penalty method as described in He et al. (2016).



285 (3) As (2), but we use continuous, piecewise quadratic ( $Q_2$ ) finite elements and an entropy viscosity stabilization technique (Guermont et al., 2011; Kronbichler et al., 2012). This is the default choice in ASPECT. In both (2) and (3) we use a BDF2 time-stepping algorithm that is second-order accurate in time to solve the advection equation (4) for the properties  $\phi_c$  (here: the density).

(4) We use the exact density as the initial condition for particles whose position we advect using a second-order accurate  
290 Runge-Kutta (RK2) algorithm. Where we need the density for the solution of the Stokes equations, we interpolate properties from particles onto a  $DGQ_2$  discontinuous finite element field and evaluate that at quadrature points as necessary.

(5) As (4), but we use RK2FOT as described in Section 3.3.

In order to limit ourselves to examining *the accuracy in time* of these five benchmark series, we will only consider a single  
295 combination of Stokes finite-element and particle interpolation algorithm in this manuscript. We will use a  $Q_2 \times Q_1$  Stokes element, and a linear least-squares particle interpolation algorithm with initially 64 particles per cell. We have described the influence of these choices in earlier work (Gassmüller et al., 2019).

## 5 Numerical evaluation of particle schemes

In the following, let us use the benchmarks derived above for the numerical evaluation of particle schemes.

### 300 5.1 Spherical shell benchmark

Fig. 3 presents the  $L_2$ -error norm of velocity, pressure, and density for the spherical annulus benchmark at a fixed time as a function of mesh resolution (left column), and at a fixed resolution as a function of time (right column).

The left column illustrates that all advection methods but RK2FOT reach second order convergence for the density with increasing resolution (bottom left panel). As expected RK2FOT is limited by the available time information and only reaches  
305 first order convergence. An additional detail is that the field methods ( $Q_2$  and  $DGQ_2$ ) have a larger error constant than the particle method (RK2), even for the same convergence rate. We will revisit the source of this error constant when discussing the error accumulation over time. Starting at moderate resolutions (around  $h = \frac{1}{16}$ ) the RK2FOT model only reaches a first order convergence rate in velocity, while  $Q_2$  and  $DGQ_2$  reach second-order and RK2 even maintains a third-order convergence rate up to very fine resolutions. This result is important, because it illustrates that particles do not uniformly generate smaller errors  
310 than field methods, but can indeed generate larger errors if their advection method is too simple and therefore inaccurate.

Analyzing the error evolution over time (the right column of Fig. 3) illustrates further differences between field and particle methods. Velocity and pressure errors reveal that RK2FOT accumulates the largest errors over time as expected, followed by  $Q_2$  and  $DGQ_2$ . RK2 accumulates the smallest errors. However, the density error norm shows distinct differences between the methods. While RK2 and RK2FOT start off at the same error value, and RK2 almost maintains this error over the evolution  
315 of the model, the error of RK2FOT increases significantly over time. The rate of increase in the RK2FOT scheme changes

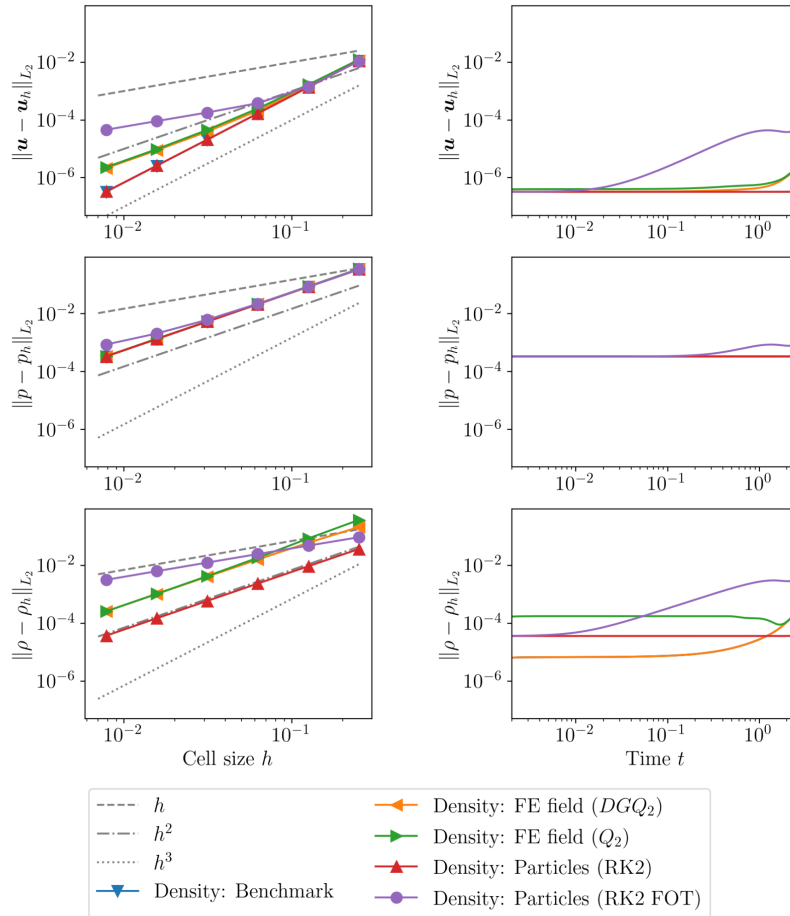


**Figure 3.** Transient spherical annulus benchmark. Left:  $L_2$  error norms of velocity (top row), pressure (middle row), and density (bottom row) for different cell sizes  $h$  at time  $t = \ln(1 + 4\pi) \approx 2.6075$ . Different colors and marker styles show different advection methods; gray lines show ideal first, second, and third order convergence. Note that the line for an exact (benchmark) density overlaps with the RK2 line. Right:  $L_2$  error norms of velocity (top row), pressure (middle row), and density (bottom row) over time for resolution  $h = 1/128$ . Colors as in left column, and the exact benchmark density line is hidden behind the RK2 case. For more details on the distinction between the RK2 case and the benchmark density case see the appendix.



towards the end of the model run. We show in Appendix B that this slowdown is related to the periodicity of our benchmark solution. The field methods  $Q_2$  and  $DGQ_2$  behave distinctly different.  $DGQ_2$  starts at a much smaller error value than all other methods, but accumulates significant errors towards the end of the model run.  $Q_2$  already starts at a significantly larger error value than all other methods. This is likely related to the fact that the used entropy viscosity method falls back to a first-order stabilization scheme for the first time step, which introduces a large amount of numerical diffusion at the model start (and only then). The overall shape of these curves is due to properties of the exact solution, not the method used, but is not of interest to us here.

Summarizing these findings, low-order particle methods show larger errors than the tested field methods, while higher-order particle methods outperform the field methods in our benchmark both with increasing resolution and with increasing model time. Therefore, whenever the other error sources of the solution are sufficiently small (i.e., if the Stokes element and time-stepping scheme allows for higher order accuracy) a higher order particle scheme can significantly enhance the accuracy of the solution. This is even true considering the higher cost of higher-order schemes. Generally, higher order schemes are more computationally expensive than lower order schemes both in number of operations and required memory. However, their higher cost is generally independent of resolution. For example RK2 requires approximately  $2 \times$  the computations that RK2FOT requires and the same amount of memory, independent of mesh size. Considering that higher-order schemes are orders of magnitude more accurate and converge faster towards the true solution, their benefits become more apparent the higher the model resolution and the larger the model end time. Therefore they are beneficial as long as the other numerical algorithms reach the same accuracy.

## 5.2 Box benchmark

The box benchmark results follow a similar pattern for the dependence of errors on the methods used, see Fig. 4. First, the solution using the analytical density solution produces a third-order convergence in velocity and second-order in pressure, which proves that the Stokes elements reach their optimal convergence order when given accurate density distributions. Second, and confirming theoretical predictions, the RK2 first-order time (RK2FOT) advection method creates a first order accurate approximation for the density, which also generates a first-order accurate pressure and velocity solution, therefore significantly limiting the potential accuracy of the Stokes elements. All other advection methods reach second-order convergence as predicted by their derivations, however with significant differences in the absolute error norm. For all solution variables, particles advected using a full RK2 scheme reach about a one order of magnitude lower error norm at the end time than the  $Q_2$  and  $DGQ_2$  finite-element methods, a value that depends on the chosen end time (compare right column of Fig. 4 and next paragraph). One feature to note is that the velocity error of the RK2 particle advection method starts with a third-order convergence rate at low resolutions and transitions to a second-order convergence rate for higher resolutions (top left panel of Fig. 4, red line with triangles). We assume that this transition is caused by a shift in the dominant error source: At large  $h$  the spatial error in the solution dominates, which is consistent with the observation that the particle solution (red line, triangles in bottom left panel of Fig. 4) is very close to the analytical density solution (blue line, circles) and converges with third order. At smaller  $h$  the spatial error reduces significantly, leaving the time error, which converges at second-order, as the remaining dominant source

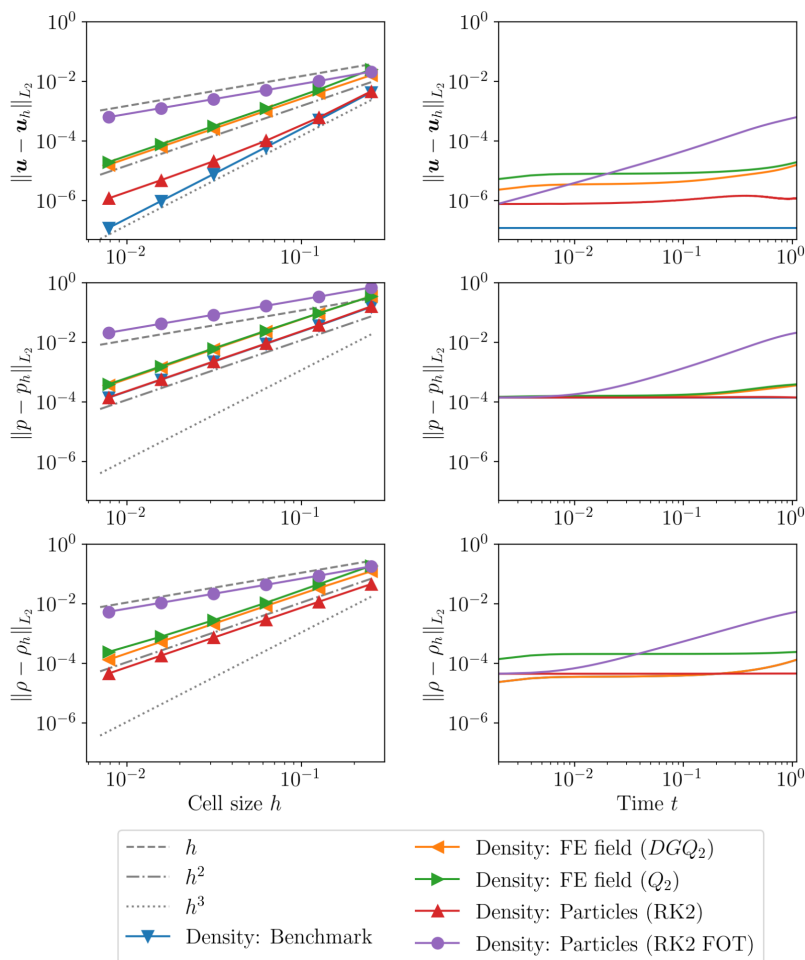


**Figure 4.** Transient box benchmark. Left:  $L_2$  error norms of velocity (top row), pressure (middle row), and density (bottom row) for different cell sizes  $h$  at time  $t = \ln(1 + 2) \approx 1.0986$ . Different colors and marker styles show different advection methods; gray lines show ideal first, second and third order convergence. Right:  $L_2$  error norms of velocity (top row), pressure (middle row), and density (bottom row) as a function of time for resolution  $h = 1/128$ .



350 of velocity error. We observed such a transition in the dominant error source already in our earlier work (Gassmöller et al., 2019).

When evaluating the error norms of the solution as a function of time for a fixed resolution (right column of Fig. 4), we can gain additional insight into the properties of the advection methods. While it is obvious that the RK2FOT methods remains the most inaccurate method at a sufficiently large time, this comparison also makes clear that it shares the same error value  
355 as RK2 at the start of the model, which is lower than the  $Q_2$  and  $DGQ_2$  methods. This is because the error in the first time step is dominated by the accuracy of the spatial approximation of the density. This also means that in benchmarks that are instantaneous or very short, the RK2FOT method will perform at nearly the same accuracy as the RK2 method, leading to misleading conclusions about its accuracy and suitability for time-dependent geodynamic models. Both  $Q_2$  and  $DGQ_2$  methods start at significantly larger errors in velocity and pressure, but accumulate less error over time than RK2FOT, although  
360 more than RK2.

For our conclusion it is important to note that even though both particle methods start with a significantly smaller error than finite-element advection methods, the first order accuracy of the RK2FOT scheme produces significantly larger errors and that this effect becomes more pronounced with increasing resolution and increasing model runtime. We conclude similar to the spherical shell case that higher order particle advection schemes outperform low order schemes in overall model accuracy, even  
365 considering their higher computational cost, as long as the Stokes solution can reach the same high accuracy of the particle method.

## 6 Application: Evolution of the mineral grain size below oceanic lithosphere

Above we have illustrated the influence of algorithmic choices on the accuracy of benchmark results. However, this does not by itself justify the increased cost of such an algorithm in practical models: Perhaps, in typical geodynamic applications, the  
370 error due to a low-order time approximation is negligible compared to other error sources and therefore a simple advection method would be sufficient. In the following, we use an application model to show that the higher accuracy is indeed important and can influence first-order outcomes and the interpretation of a geodynamic study.

In order to illustrate this point, we use an example where the property carried on the particles (the grain size  $d$ ) nonlinearly influences the material properties (the viscosity  $\eta$ ) and the corresponding solution of the equations. Our model setup (Fig. 5,  
375 top) consists of the oceanic lithosphere and asthenosphere, down to a depth of 410 km, moving away from a spreading center at the top left corner of the model and horizontally extending to a distance of 4000 km from the ridge. The plate speed is prescribed in horizontal direction to 5 cm/yr at the top, and right (outflow) boundary and linearly decreases with depth starting at 100 km towards 0 cm/yr at the bottom of the model; the left (ridge axis) boundary of the model is closed and stress-free (free-slip). The vertical velocity component is not prescribed at the bottom and right boundary, instead a depth-dependent  
380 hydrostatic pressure profile that is computed at the model start and is constant in time is prescribed. Therefore, material can flow in beneath the ridge axis and leaves the model either through the bottom or the right boundary. The initial temperature follows an adiabatic profile with a potential temperature of 1623 K, and a half-space cooling profile close to the top boundary



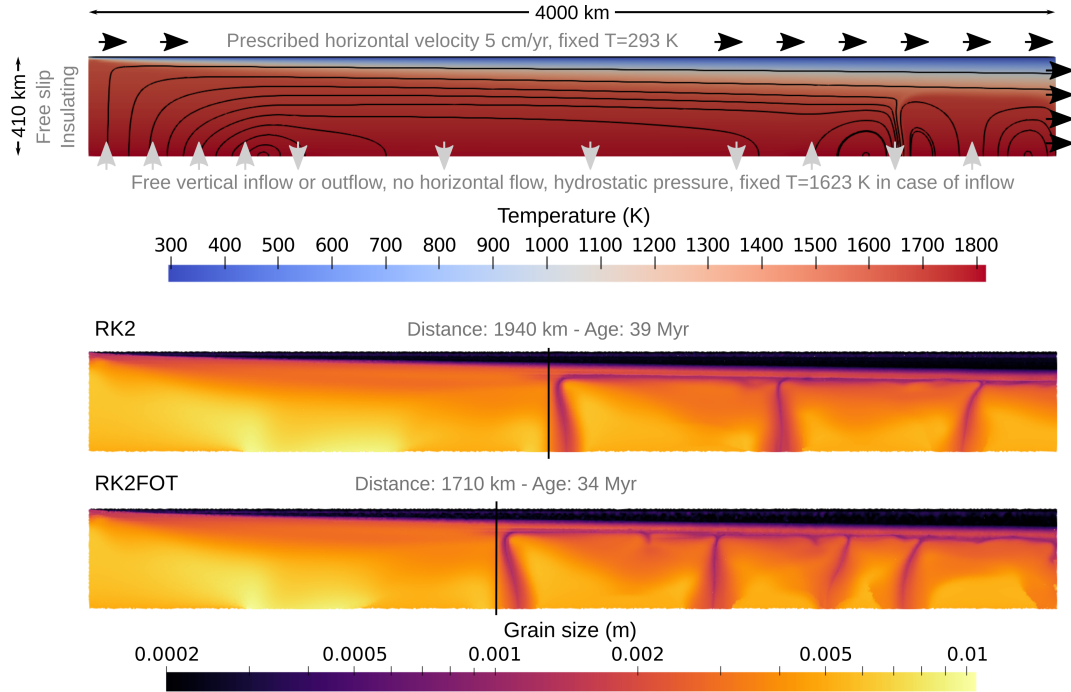


**Figure 5.** Top: Setup of the application model. Background colors illustrate temperature, black solid lines are streamlines. Arrows indicate velocity. Center and bottom: Grain size at the end of the model run after 200 million years, in a model that uses the second-order in time Runge–Kutta scheme (center), and the first-order in time Runge–Kutta scheme (bottom).

with an age consistent with the plate velocity. The initial temperature also includes a small ( $r = 10 \text{ km}$ ) thermal perturbation at the ridge axis to support the onset of spreading. The initial grain size is set to  $d = 5 \text{ mm}$ , and also includes a small ( $r = 30 \text{ km}$ ) anomaly close to the ridge axis. Since the temperature is prescribed at the top boundary, the plate is cooling conductively over time until small-scale convection sets in at the base of the plate.

In this model, we use particles to carry information about the mineral grain size  $d$ , which influences the viscosity nonlinearly as

$$\eta_{\text{diff}} = \frac{1}{2} A_{\text{diff}}^{-1} d^m \exp\left(\frac{E_{\text{diff}} + PV_{\text{diff}}}{RT}\right), \quad (26)$$

$$\eta_{\text{dis}} = \frac{1}{2} A_{\text{dis}}^{-\frac{1}{n}} \dot{\epsilon}_{\text{dis,II}}^{\frac{1-n}{n}} \exp\left(\frac{E_{\text{dis}} + PV_{\text{dis}}}{nRT}\right), \quad (27)$$

resulting in an effective viscosity of

$$\eta_{\text{eff}} = \frac{\eta_{\text{diff}} \eta_{\text{dis}}}{\eta_{\text{diff}} + \eta_{\text{dis}}}. \quad (28)$$

Here,  $\eta_{\text{diff}}$ ,  $\eta_{\text{dis}}$ , and  $\eta_{\text{eff}}$  are the diffusion, dislocation and effective viscosity, respectively.  $A_{\text{diff}} = 5 \times 10^{-15} \text{ m}^3/\text{Pa/s}$  and  $A_{\text{dis}} = 10^{-15} \text{ Pa}^{-3.5}/\text{s}$  are diffusion and dislocation creep prefactors,  $E_{\text{diff}} = 375 \text{ kJ/mol}$  and  $E_{\text{dis}} = 530 \text{ kJ/mol}$  the activation



395 energy for diffusion and dislocation creep,  $V_{\text{diff}} = 4 \times 10^{-6} \text{ m}^3/\text{mol}$  and  $V_{\text{dis}} = 1.4 \times 10^{-5} \text{ m}^3/\text{mol}$  the respective activation volumes;  $R$  the universal gas constant,  $P$  the pressure,  $T$  the temperature,  $m = 3$  the grain size exponent of diffusion creep,  $\varepsilon_{\text{dis,II}}$  the square-root of the second moment invariant of the dislocation strain rate, and  $n = 3.5$  the dislocation creep strain rate exponent. We limit the viscosity computed in (28) to be between  $10^{16}$  and  $10^{23} \text{ Pa s}$ .

In addition, particles are not just advected, but both the temperature and the strain rate in the model influence the evolution  
 400 of the grain size. For a single particle moving along the flow field, we describe this evolution via the equation

$$\frac{d}{dt}d(t) = p_g^{-1} d^{1-p_g} k_g \exp\left(-\frac{E_g + PV_g}{RT}\right) - 4\dot{\varepsilon}_{\text{II}} \dot{\varepsilon}_{\text{dis,II}} \eta_{\text{eff}} \frac{\lambda d^2}{c\gamma}, \quad (29)$$

which implies that the grain size *field*  $d(\mathbf{x}, t)$  satisfies the equation

$$\left(\frac{\partial d}{\partial t} + \mathbf{u} \cdot \nabla d\right) = p_g^{-1} d^{1-p_g} k_g \exp\left(-\frac{E_g + PV_g}{RT}\right) - 4\dot{\varepsilon}_{\text{II}} \dot{\varepsilon}_{\text{dis,II}} \eta_{\text{eff}} \frac{\lambda d^2}{c\gamma}. \quad (30)$$

Here,  $k_g = 1.92 \times 10^{-10} \text{ m}^3/\text{s}$  is the grain size growth prefactor,  $E_g = 400 \text{ kJ/mol}$  and  $V_g = 0 \text{ m}^3/\text{mol}$  the activation energy  
 405 and volume for grain size growth respectively.  $p_g = 3$  is the grain size growth exponent,  $c = 3$  a geometric constant,  $\lambda = 0.1$  the fraction of deformation work that goes into changing the grain boundary area and  $\gamma = 1$  the average specific grain boundary energy. For a detailed discussion of these terms and all parameter values we refer to (Dannberg et al., 2017). The terms on the right-hand sides of these equation describe how the dynamic grain size increases over time (with a non-linear dependence on temperature and grain size itself) and how it is decreased by dynamic recrystallization due to strain accomodated by dislocation  
 410 creep (which depends nonlinearly on stress and temperature).

We solve this model using only the particle-based RK2 and RK2FOT advection schemes. As can be seen in the bottom two panels of Fig. 5, the two schemes produce noticeably different locations of onset of convection. While the model with a full RK2 advection scheme develops small-scale convection beneath the oceanic plate at a distance of 1940 km from the ridge, the model with RK2FOT develops the onset at 1710 km distance, corresponding to plate ages of 39 Myr (RK2) and 34 Myr  
 415 (RK2FOT), respectively. More importantly, the different outcomes between the advection methods is not just a temporary state at this precise time, but the models stabilize around this solution, meaning that the onset of small-scale convection is systematically earlier in the model with a first-order accurate advection scheme. This difference is relevant because the exact timing of onset is important for the argument that small-scale convection causes a flattening of topography in seafloor subsidence datasets, and therefore ultimately for the plate model of oceanic lithosphere cooling (Stein and Stein, 1992; Huang  
 420 and Zhong, 2005; Richards et al., 2018). In addition to the difference in onset of convection, the characteristic length scale at which instabilities develop below the lithosphere is significantly smaller for the RK2FOT method, visible in the larger number and smaller distance between convection cells in the bottom panel of Fig. 5. This is especially relevant as the distance between seismic anomalies associated with small-scale convection is a constraint from seismic studies and can be used to validate geodynamic models (Eilon et al., 2022). We want to emphasize here that our model is conceptual and not intended to produce  
 425 realistic timings or length scales, but rather that a misprediction of these quantities due to inaccurate particle algorithms in models has concrete consequences for the interpretation of geodynamic features observed on Earth.



Because both the onset of small-scale convection and the length scale of convection cells is governed by the growth of small instabilities in a boundary layer, it is reasonable to assume that the lower accuracy of RK2FOT supports this growth of instabilities and explains the earlier onset of convection. The growth of instabilities in a boundary layer (or internally layered systems) is one of the most common processes for developing flow features in convecting systems like the Earth's mantle and lithosphere. Examples are the generation of plumes at the core-mantle boundary, the stagnation of subducted slabs or plumes at phase transitions or the initiation of plate boundaries in models of lithosphere dynamics. We therefore infer from our benchmark results that models of all of these processes can benefit from incorporating more accurate particle advection methods, and that predictions of models using lower order advection schemes may need to be adjusted or reproduced in higher resolution studies.

## 7 Conclusions

In our benchmarks and application models we have shown that implementing accurate particle algorithms, in particular higher-order in time, can significantly increase the numerical accuracy of geodynamic models. One of the conclusions of our benchmarks is that commonly used particle advection methods that are higher order in space but first order in time acquire significant amounts of numerical error in time-variable flow, which becomes more pronounced the higher the resolution and the longer the model run. The reason this error is not often discussed in the geodynamic literature is that traditional benchmarks that either rely on instantaneous analytical solutions, or on steady-state solutions, cannot show this error by their design. Only model comparison studies or benchmarks with analytical solutions in transient flow can point out this error source. Given that many geodynamic finite-element models already use Stokes elements that allow for higher order accuracy to ensure stability (e.g. Taylor-Hood  $Q_2 \times Q_1$  or  $Q_2 \times P_{-1}$ ), it would be straightforward to extend their particle advection algorithms to a second-order in time method. While this can increase the cost for evaluating velocities at the particle locations, our results show that the increased convergence order and improved accuracy of the model results is well worth the additional cost. Of course in order to increase the overall model accuracy, all other employed algorithms need to support the same accuracy.

We believe that a sharper focus on quantifying the numerical accuracy of geodynamic models will generate more trust in geodynamic model solutions and increase the impact of the discipline of geodynamic modeling as a whole. We provide the reference implementation of our algorithms and benchmarks in the open-source community software ASPECT and hope that they are useful to the community at large.

*Code availability.* Computations were done using the ASPECT code (Heister et al., 2017; Kronbichler et al., 2012; Bangerth et al., 2023, 2022) version 2.6.0-pre (git hash 299a6456385b1fde6564fc079f3aa01cac075f24). ASPECT is published under the GPL2 license, and the necessary data to reproduce the benchmark models is included in the software. The precise ASPECT version and the model setup for Section 6 is published on Zenodo as Gassmüller (2023).



*Author contributions.* R.G. devised the study, adapted the benchmark cases, and wrote the majority of the manuscript. J.D. provided and described the grain-size application model. W.B. developed the integrator error analysis. E.G.P. provided the particle interpolation algorithm. E.G.P. and C.T. developed the instantaneous solution of the annulus benchmark case. All authors jointly interpreted the results and improved the manuscript.

*Competing interests.* The authors declare that they have no conflict of interest.

*Acknowledgements.* The authors acknowledge University of Florida Research Computing (<http://researchcomputing.ufl.edu>) for providing computational resources and support that have contributed to the research results reported in this publication. Computations were also run on the Stampede2 system at the Texas Advanced Computing Center (TACC) as part of award TG-EAR080022N.

We thank the Computational Infrastructure for Geodynamics (<https://geodynamics.org>) – funded by the National Science Foundation under awards EAR-1550901, and EAR-2149126 – for supporting the development of ASPECT.

R. Gassmüller and W. Bangerth were partially supported by the National Science Foundation under award OCI-1148116 as part of the Software Infrastructure for Sustained Innovation (SI2) program; and by the Computational Infrastructure in Geodynamics initiative (CIG), through the National Science Foundation under Awards No. EAR-0949446, EAR-1550901, EAR-2149126. W. Bangerth was also supported by the National Science Foundation under Awards OAC-1835673 and EAR-1925595.

E. G. Puckett was supported by the National Science Foundation under Award ACI-1440811 as part of the SI2 Scientific Software Elements (SSE) program.

J. Dannberg and R. Gassmüller were supported by the National Science Foundation under awards EAR-1925677 and EAR-2054605.

## Appendix A: Derivation of an exact solution in an annulus

We begin by deriving an exact solution to the stationary, incompressible Stokes equations for an isoviscous, isothermal fluid in a two-dimensional annulus. Given the geometry of the problem, we work in polar coordinates. We denote the orthonormal basis vectors by  $\mathbf{e}_r$  and  $\mathbf{e}_\theta$ , the inner radius of the annulus by  $R_1$  and the outer radius by  $R_2$ . Further, we assume that the viscosity is a constant  $\eta = 1$ , and set the gravity vector to an inward-pointing vector  $\mathbf{g} = -g_r \mathbf{e}_r$ , with  $g_r = 1$ .

Given these assumptions, the incompressible Stokes equations in the annulus are (Schubert et al., 2001)

$$\frac{\partial^2 v_r}{\partial r^2} + \frac{1}{r} \frac{\partial v_r}{\partial r} + \frac{1}{r^2} \frac{\partial^2 v_r}{\partial \theta^2} - \frac{v_r}{r^2} - \frac{2}{r^2} \frac{\partial v_\theta}{\partial \theta} - \frac{\partial p}{\partial r} - \rho g_r = 0 \quad (\text{A1})$$

$$\frac{\partial^2 v_\theta}{\partial r^2} + \frac{1}{r} \frac{\partial v_\theta}{\partial r} + \frac{1}{r^2} \frac{\partial^2 v_\theta}{\partial \theta^2} + \frac{2}{r^2} \frac{\partial v_r}{\partial \theta} - \frac{v_\theta}{r^2} - \frac{1}{r} \frac{\partial p}{\partial \theta} = 0 \quad (\text{A2})$$

$$\frac{1}{r} \frac{\partial (r v_r)}{\partial r} + \frac{1}{r} \frac{\partial v_\theta}{\partial \theta} = 0. \quad (\text{A3})$$

Equations (A1) and (A2) are the momentum equations in polar coordinates while equation (A3) is the incompressibility constraint.



485 We then seek solutions whose circumferential velocity can be written as

$$v_{\theta}(r, \theta) = f(r) \cos(k\theta) \quad (\text{A4})$$

where  $k$  is an integer and where  $f(r)$  will be specified later. From equation (A3) we then obtain

$$\frac{\partial(rv_r)}{\partial r} = -\frac{\partial v_{\theta}}{\partial \theta} = kf(r) \sin(k\theta), \quad (\text{A5})$$

leading to

490  $v_r(r, \theta) = g(r)k \sin(k\theta), \quad (\text{A6})$

where

$$g(r) = \frac{1}{r} \int^r f(r') dr'. \quad (\text{A7})$$

Since we want to fix the velocity to be tangential at both boundaries we have

$$v_r(R_1, \theta) = v_r(R_2, \theta) = 0 \quad (\text{A8})$$

495 for all  $\theta \in [0, 2\pi]$ . We choose

$$f(r) = Ar + B/r \quad (\text{A9})$$

in analogy to the solution of the Laplace equation in Chapter 6 of (Strauss, 2007), and thus

$$g(r) = \frac{A}{2}r + \frac{B}{r} \ln r + \frac{C}{r} \quad (\text{A10})$$

where  $C$  is a non-zero constant of integration. Given the boundary conditions in equation A8 we find that

500  $A = -C \frac{2(\ln R_1 - \ln R_2)}{R_2^2 \ln R_1 - R_1^2 \ln R_2}, \quad B = -C \frac{R_2^2 - R_1^2}{R_2^2 \ln R_1 - R_1^2 \ln R_2}. \quad (\text{A11})$

In this work we choose  $C = -1$ . Our earlier choice of  $f$  means that

$$\frac{\partial^2 f}{\partial r^2} + \frac{1}{r} \frac{\partial f}{\partial r} - \frac{f}{r^2} = 0, \quad (\text{A12})$$

so that equation (A2) simplifies to

$$\frac{1}{r^2} \frac{\partial^2 v_{\theta}}{\partial \theta^2} + \frac{2}{r^2} \frac{\partial v_r}{\partial \theta} - \frac{1}{r} \frac{\partial p}{\partial \theta} = 0, \quad (\text{A13})$$

505 which together with (A4) leads to

$$p(r, \theta) = kh(r) \sin(k\theta) + l(r), \quad (\text{A14})$$



where  $l(r)$  comes from integration with respect to  $\theta$  and  $h(r) = (2g(r) - f(r))/r$ . We now insert equation (A14) into equation (A1) to obtain

$$\begin{aligned}
 \rho(r, \theta) &= \frac{\partial^2 v_r}{\partial r^2} + \frac{1}{r} \frac{\partial v_r}{\partial r} + \frac{1}{r^2} \frac{\partial^2 v_r}{\partial \theta^2} - \frac{v_r}{r^2} - \frac{2}{r^2} \frac{\partial v_\theta}{\partial \theta} - \frac{\partial p}{\partial r} \\
 510 \quad &= kg''(r) \sin(k\theta) + k \frac{g'(r)}{r} \sin(k\theta) - k^3 \frac{g(r)}{r^2} \sin(k\theta) \\
 &\quad - k \frac{g(r)}{r^2} \sin(k\theta) + k \frac{2f(r)}{r^2} \sin(k\theta) - kh'(r) \sin(k\theta) - l'(r), \\
 &= m(r)k \sin(k\theta) - l'(r)
 \end{aligned} \tag{A15}$$

with

$$m(r) = g'' - \frac{g'}{r} - \frac{g}{r^2}(k^2 - 1) + \frac{f}{r^2} + \frac{f'}{r} \tag{A16}$$

$$515 \quad = -\frac{f-g}{r^2} + \frac{f'-g'}{r} - \frac{f-g}{r^2} - \frac{g}{r^2}(k^2 - 1) + \frac{f}{r^2} + \frac{f'}{r} \tag{A17}$$

$$= -\frac{f-g}{r^2} + \frac{f'}{r} - \frac{f-g}{r^2} - \frac{f-g}{r^2} - \frac{g}{r^2}(k^2 - 1) + \frac{f}{r^2} + \frac{f'}{r} \tag{A18}$$

$$= -3\frac{f-g}{r^2} + \frac{f'}{r} - \frac{g}{r^2}(k^2 - 1) + \frac{f}{r^2} + \frac{f'}{r} \tag{A19}$$

since it is easy to verify using (A7) that  $g'(r) = (f - g)/r$ .

Taking  $k = 0$  yields  $\rho(r, \theta) = -l'(r)$ , so we choose  $l'(r) = -\rho_0$ . In this case,

$$520 \quad p(r, \theta)|_{k=0} = l(r) = \rho_0 g_r (R_2 - r), \tag{A20}$$

which represents a familiar linear pressure increase with depth for constant density and gravity, and where we have imposed  $p(r, \theta) = 0$  at the outer radius  $r = R_2$ .

In summary, equations (A4), (A6), and (A14) form a solution of the incompressible Stokes equations, which fully stated reads

$$525 \quad v_\theta(r, \theta) = f(r) \cos(k\theta), \tag{A21}$$

$$v_r(r, \theta) = g(r)k \sin(k\theta), \tag{A22}$$

$$p(r, \theta) = kh(r) \sin(k\theta) + \rho_0 g_r (R_2 - r), \tag{A23}$$



with

$$\rho(r, \theta) = m(r)k \sin(k\theta) + \rho_0, \quad (\text{A24})$$

$$530 \quad g_r = 1, \quad (\text{A25})$$

$$g_\theta = 0, \quad (\text{A26})$$

$$f(r) = Ar + B/r, \quad (\text{A27})$$

$$g(r) = \frac{A}{2}r + \frac{B}{r} \ln r + \frac{C}{r}, \quad (\text{A28})$$

$$h(r) = \frac{2g(r) - f(r)}{r}, \quad (\text{A29})$$

$$535 \quad m(r) = g''(r) - \frac{g'(r)}{r} - \frac{g(r)}{r^2}(k^2 - 1) + \frac{f(r)}{r^2} + \frac{f'(r)}{r}, \quad (\text{A30})$$

$$A = -C \frac{2(\ln R_1 - \ln R_2)}{R_2^2 \ln R_1 - R_1^2 \ln R_2}, \quad (\text{A31})$$

$$B = -C \frac{R_2^2 - R_1^2}{R_2^2 \ln R_1 - R_1^2 \ln R_2}, \quad (\text{A32})$$

$$C = -1. \quad (\text{A33})$$

We can use the velocity solution for  $v_r$  and  $v_\theta$  to determine a stream function for this flow field, which will be used to derive  
 540 the stationary benchmark below:

$$\Psi(r, \theta) = - \left( \frac{A}{2}r^2 + B \ln(r) + C \right) \cos(k\theta). \quad (\text{A34})$$

The solution above is time-independent and only valid for instantaneous models where the density is not advected. To make  
 it time-dependent, we first modify the density and gravity to create a steady-state variant of the benchmark and add a known  
 time-dependent component to the velocity as described in Section 4. We start by choosing a density field consistent with the  
 545 streamline  $\rho(r, \theta) = \Psi(r, \theta)$ . In our concrete benchmark this solution no longer satisfies the derived Stokes solution. However,  
 we can recover an analytic solution by exploiting the fact that for the incompressible Stokes equations the density  $\rho$  only enters  
 the computation as a product with the gravity  $\mathbf{g}$ . Therefore, if as described in the example case above  $m(r)k \sin(k\theta)$  is the  
 right hand side force term that satisfies the Stokes equation, we can still choose the density arbitrarily (e.g.  $\rho(r, \theta) = \Psi(r, \theta)$ ),  
 as long as we define the gravity to be  $\mathbf{g}(r, \theta) = m(r)k \sin(k\theta)/\rho(r, \theta)$ . This keeps the original forcing term constant, and so  
 550 makes the solution independent of time. The steady-state solution therefore is the same as above, except:

$$\rho(r, \theta) = \Psi(r, \theta), \quad (\text{A35})$$

$$g_r(r, \theta) = m(r)k \sin(k\theta)/\rho(r, \theta), \quad (\text{A36})$$

with all other constants chosen as before.

In order to transform this steady-state benchmark into a known transient solution we then add a solid body rotation with  
 555 a nonlinear time-dependent rotational velocity to the flow field. Since solid body rotations lie in the nullspace of the incom-  
 pressible Stokes equations on an annular domain, the resulting flow field will still be a solution of the incompressible Stokes

equations. This approach will work as long as we perform an appropriate rotation of all components of the solution, and is equivalent to defining the solution in a rotating reference frame. We therefore modify the velocity components in  $\theta$  direction to

$$560 \quad v_{\theta}(r, \theta, t) = f(r) \cos(k(\theta - \tau(t))) + r\omega(t). \quad (\text{A37})$$

Here  $\tau(t)$  is a phase shift, and  $\omega(t)$  is an angular velocity. The phase shift  $\tau(t)$  can be computed as the time integral of the angular velocity from the beginning of the model up to the present time  $t$ :

$$\tau(t) = \int_0^t \omega(s) ds. \quad (\text{A38})$$

In order to not make the problem too simple, we forgo the case of a constant angular velocity and instead choose  $\omega(t) = e^t$ ,  
 565 resulting in  $\tau(t) = e^t - 1$ .

Since the modification of the velocity in (A37) by the solid body rotation  $r\omega(t)$  lies in the nullspace of the Stokes equations, it is straightforward to compute the modifications of the remaining solution variables, which only involves adding the phase shift to the  $\theta$  coordinate.

The final consideration is how to achieve this prescribed rotation in the model. Since in the incompressible Stokes equations  
 570 stresses are transmitted instantaneously throughout the entire domain, we can use the exact, known velocities as boundary conditions and expect the motion to apply equally to the entire model domain.

## Appendix B: Detailed error investigation of the spherical shell benchmark

In order to better understand the accuracy of the RK2 method and investigate the source of the error decrease late in the model we show in Fig. B1 a detailed comparison of only RK2 against the analytical density method. In order to visualize  
 575 the difference between RK2 and analytical density over resolution (left column) we no longer plot the absolute error in the  $L_2$  norm, but instead the relative difference in error between RK2 and analytical density; i.e., if  $\epsilon_{RK2} = \|\mathbf{u} - \mathbf{u}_h^{RK2}\|_{L_2}$  and  $\epsilon_{AD} = \|\mathbf{u} - \mathbf{u}_h^{AD}\|_{L_2}$  then we plot  $(\epsilon_{RK2} - \epsilon_{AD})/\epsilon_{AD}$ . This way of plotting the error illustrates if both error values converge at the same rate – leading to a constant relative difference between the two errors – or if the RK2 error indeed converges at a lower rate – leading to a linearly (or higher-order) increasing relative error difference towards smaller  $h$ . As it turns out the  
 580 relative error indeed increases linearly with resolution, meaning that RK2 converges at only second order, however the second order contribution is so small that it is not yet visible in the corresponding plot of Fig. 3. On the other hand, the pressure (left column, middle row), converges at the same second order rate for both analytical density and RK2, leading to a constant relative difference between the two errors.

Turning to the evolution of error over model time (Fig. B1, right column) reveals that what looked like a constant error value  
 585 in Fig. 3 indeed follows the same trends as the other methods, only at drastically reduced error values. While the error values for velocity and density increased by 1-2 orders of magnitude from model start to end for the other advection methods (RK2FOT,



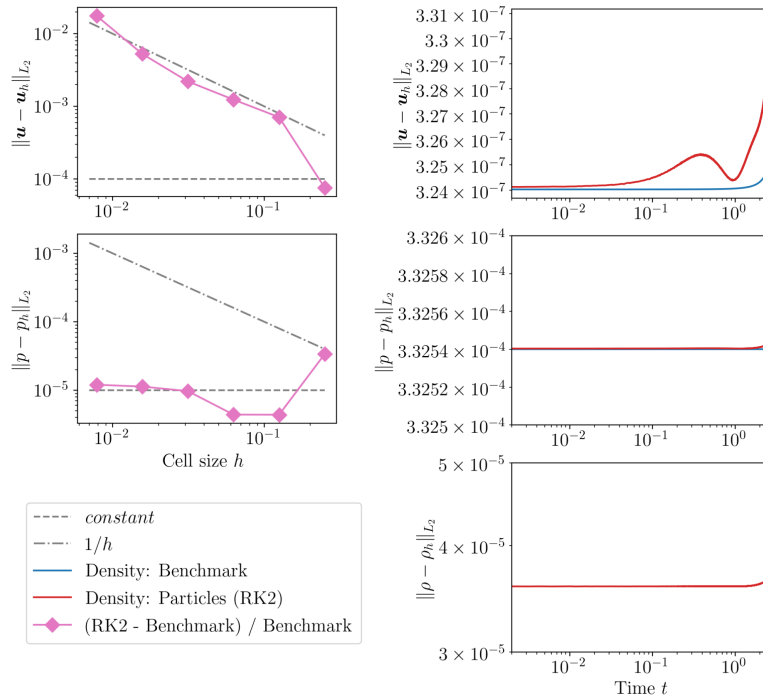


**Figure B1.** Transient spherical annulus benchmark. Left:  $L_2$  error norms of velocity (top row) and pressure (middle row) for different cell sizes  $h$  at time  $t = \ln(1+4\pi) \approx 2.6075$ . The pink line shows the relative difference in the error between RK2 and the analytical density model. Gray lines indicate the same convergence order (dashed line), or one convergence order lower (dash-dotted line) than the analytical density model. Right:  $L_2$  error norms of velocity (top row), pressure (middle row), and density (bottom row) as a function of time for resolution  $h = 1/128$  for analytical density and RK2 model.

$Q_2$ ,  $DGQ_2$ ), they increase by at most  $\approx 2\%$  for RK2. Additionally, RK2 features the same error reduction close to  $t = 1$  as the other methods. Finally, it becomes apparent that even the model using analytical densities features a small but growing velocity error. Because the density error in this model is zero (analytical density) it seems reasonable to assume this error is a result of the Stokes solver. The accuracy of the Stokes solver depends on the absolute value of velocity, which increases exponentially over time. In other words the blue line in the top right panel of Fig. B1 represents the best possible accuracy any advection method could reach for the given Stokes solver if it transported material information with perfect accuracy. Considering all the results presented in this section, we consider the RK2 scheme to be very close to achieving this theoretical limit.

To understand the reduction in velocity error and density error at certain model times requires us to take a closer look at the benchmark solution. Particularly relevant is that the benchmark solution is rotation-symmetric, with 4 regions of upwelling and 4 regions of downwelling. Therefore, rotating the density field by 90 degrees at any given time would lead to exactly the same solution. For some reason the reduction in velocity error in RK2 coincides almost exactly with a quarter rotation of the model solution at  $t = \ln(1 + \pi/2) \approx 0.944$ , the reduction for  $Q_2$  coincides with a rotation by three quarters of a rotation ( $t =$



600  $\ln(1+3\pi/2) \approx 1.742$ ), and the reduction for RK2FOT coincides with a full rotation ( $t = \ln(1+2\pi) \approx 1.985$ ). We speculate that  
the times of rotation symmetry with the starting solution allows for a resonance between the accumulated error in the numerical  
solution and the analytical solution at a slightly different time. This interaction would allow for an apparent reduction in error  
that does not actually exist, which is consistent with the observation that all errors rapidly increase again after the minimum.  
However, while this theory explains why reductions in error could happen at specific times, we have no explanation why the  
anomaly happens at different multiples of the rotation symmetry for different advection methods. We can only speculate that  
605 the occurrence depends on a very specific feature in each model, for example how close individual discrete time steps end at the  
analytically determined times of rotation symmetry. Independent of the origin of the anomaly, the results of the convergence  
studies show that it does not influence the measurement of the convergence orders of different methods.



## References

- Arndt, D., Fehn, N., Kanschä, G., Kormann, K., Kronbichler, M., Munch, P., Wall, W. A., and Witte, J.: ExaDG: High-Order Discontinuous Galerkin for the Exa-Scale, in: *Software for Exascale Computing - SPPEXA 2016-2019*, edited by Bungartz, H.-J., Reiz, S., Uekermann, B., Neumann, P., and Nagel, W. E., pp. 189–224, Springer International Publishing, Cham, 2020.
- Arndt, D., Bangerth, W., Bergbauer, M., Feder, M., Fehling, M., Heinz, J., Heister, T., Heltai, L., Kronbichler, M., Maier, M., Munch, P., Pelteret, J.-P., Turcksin, B., Wells, D., and Zampini, S.: The deal.II Library, Version 9.5, *Journal of Numerical Mathematics*, 31, 231–246, <https://doi.org/10.1515/jnma-2023-0089>, 2023.
- Arnould, M., Coltice, N., Flament, N., and Mallard, C.: Plate tectonics and mantle controls on plume dynamics, *Earth and Planetary Science Letters*, 547, 116 439, 2020.
- Baes, M., Sobolev, S., Gerya, T., and Brune, S.: Plume-Induced Subduction Initiation: Single-Slab or Multi-Slab Subduction?, *Geochemistry, Geophysics, Geosystems*, 21, e2019GC008 663, 2020.
- Bangerth, W., Dannberg, J., Gasmöller, R., Heister, T., et al.: ASPECT: Advanced Solver for Problems in Earth’s ConvecTion, Computational Infrastructure in Geodynamics, <https://aspect.dealii.org/>, 2022.
- Bangerth, W., Dannberg, J., Fraters, M., Gasmöeller, R., Glerum, A., Heister, T., Myhill, R., and Naliboff, J.: ASPECT v2.5.0, <https://doi.org/10.5281/zenodo.8200213>, 2023.
- Dannberg, J., Eilon, Z., Faul, U., Gasmöller, R., Moulik, P., and Myhill, R.: The importance of grain size to mantle dynamics and seismological observations, *Geochemistry, Geophysics, Geosystems*, 18, 3034–3061, 2017.
- Duretz, T., May, D. A., Gerya, T. V., and Tackley, P. J.: Discretization errors and free surface stabilization in the finite difference and marker-in-cell method for applied geodynamics: A numerical study, *Geochemistry, Geophysics, Geosystems*, 12, <https://doi.org/10.1029/2011GC003567>, Q07004, 2011.
- Eilon, Z. C., Zhang, L., Gaherty, J. B., Forsyth, D. W., and Russell, J. B.: Sub-Lithospheric Small-Scale Convection Tomographically Imaged Beneath the Pacific Plate, *Geophysical Research Letters*, 49, e2022GL100 351, 2022.
- El Geitani, T., Golshan, S., and Blais, B.: Toward High-Order CFD-DEM: Development and Validation, *Industrial & Engineering Chemistry Research*, 62, 1141–1159, <https://doi.org/10.1021/acs.iecr.2c03546>, 2023.
- Gasmöller, R.: Benchmarking the accuracy of higher order particle methods in geodynamic models of transient flow: Data, <https://doi.org/10.5281/zenodo.10161412>, 2023.
- Gasmöller, R., Lokavarapu, H., Heien, E., Puckett, E. G., and Bangerth, W.: Flexible and scalable particle-in-cell methods with adaptive mesh refinement for geodynamic computations, *Geochemistry, Geophysics, Geosystems*, 19, 3596–3604, 2018.
- Gasmöller, R., Lokavarapu, H., Bangerth, W., and Puckett, E. G.: Evaluating the accuracy of hybrid finite element/particle-in-cell methods for modelling incompressible Stokes flow, *Geophysical Journal International*, 219, 1915–1938, 2019.
- Gerya, T. V. and Yuen, D. A.: Characteristics-based marker-in-cell method with conservative finite-differences schemes for modeling geological flows with strongly variable transport properties, *Physics of the Earth and Planetary Interiors*, 140, 293–318, 2003.
- Glerum, A., Brune, S., Stamps, D. S., and Strecker, M. R.: Victoria continental microplate dynamics controlled by the lithospheric strength distribution of the East African Rift, *Nature communications*, 11, 1–15, 2020.
- Golshan, S. and Blais, B.: Load-Balancing Strategies in Discrete Element Method Simulations, *Processes*, 10, 79, <https://doi.org/10.3390/pr10010079>, 2022.



- 645 Golshan, S., Munch, P., Gassmöller, R., Kronbichler, M., and Blais, B.: Lethe-DEM: An open-source parallel discrete element solver with  
load balancing, *Computational Particle Mechanics*, pp. 1–20, 2022.
- Grima, A. G., Lithgow-Bertelloni, C., and Cramer, F.: Orphaning regimes: the missing link between flattened and penetrating slab mor-  
phologies, *Frontiers in Earth Science*, 8, 374, 2020.
- Guermund, J.-L., Pasquetti, R., and Popov, B.: Entropy viscosity method for nonlinear conservation laws, *J. Comput. Phys.*, 230, 4248–4267,  
2011.
- 650 Gülcher, A. J. P., Ballmer, M. D., and Tackley, P. J.: Coupled dynamics and evolution of primordial and recycled heterogeneity in Earth’s  
lower mantle, *Solid Earth*, 12, 2087–2107, 2021.
- Hairer, E. and Wanner, G.: *Solving Ordinary Differential Equations II. Stiff and Differential-Algebraic Problems*, Springer-Verlag, Berlin,  
1991.
- He, Y., Puckett, E. G., and Billen, M. I.: A Discontinuous Galerkin Method with a Bound Preserving Limiter for  
655 the Advection of non-Diffusive Fields in Solid Earth Geodynamics, *Physics of the Earth and Planetary Interiors*,  
<https://doi.org/http://dx.doi.org/10.1016/j.pepi.2016.12.001>, 2016.
- Heister, T., Dannberg, J., Gassmöller, R., and Bangerth, W.: High accuracy mantle convection simulation through modern numerical methods.  
II: Realistic models and problems, *Geophysical Journal International*, 210, 833–851, 2017.
- Huang, J. and Zhong, S.: Sublithospheric small-scale convection and its implications for the residual topography at old ocean basins and the  
660 plate model, *Journal of Geophysical Research: Solid Earth*, 110, 2005.
- Jones, T. D., Sime, N., and van Keken, P.: Burying Earth’s primitive mantle in the slab graveyard, *Geochemistry, Geophysics, Geosystems*,  
22, e2020GC009396, 2021.
- Kramer, S. C., Davies, D. R., and Wilson, C. R.: Analytical solutions for mantle flow in cylindrical and spherical shells, *Geoscientific Model  
Development*, 14, 1899–1919, <https://doi.org/10.5194/gmd-14-1899-2021>, 2021.
- 665 Kronbichler, M., Heister, T., and Bangerth, W.: High Accuracy Mantle Convection Simulation through Modern Numerical Methods, *Geo-  
physics Journal International*, 191, 12–29, 2012.
- McNamara, A. K. and Zhong, S.: Thermochemical structures within a spherical mantle: Superplumes or piles?, *Journal of Geophysical  
Research*, 109, 1–14, <https://doi.org/10.1029/2003JB002847>, 2004.
- Murer, M., Formica, G., Milicchio, F., Morganti, S., and Auricchio, F.: A coupled multiphase Lagrangian-Eulerian fluid-dynamics framework  
670 for numerical simulation of Laser Metal Deposition process, *The International Journal of Advanced Manufacturing Technology*, 120,  
3269–3286, <https://doi.org/10.1007/s00170-022-08763-7>, 2022.
- Popov, A. and Marchevsky, I.: MPI-Based PFEM-2 Method Solver for Convection-Dominated CFD Problems, in: *International Conference  
on Parallel Computational Technologies*, pp. 261–275, Springer, 2022.
- Puckett, E. G., Turcotte, D. L., He, Y., Lokavarapu, H., Robey, J. M., and Kellogg, L. H.: New numerical approaches for modeling thermo-  
675 chemical convection in a compositionally stratified fluid, *Physics of the Earth and Planetary Interiors*, 276, 10–35, 2018.
- Pusok, A. E., Kaus, B. J., and Popov, A. A.: On the quality of velocity interpolation schemes for marker-in-cell method and staggered grids,  
*Pure and Applied Geophysics*, 174, 1071–1089, 2017.
- Richards, F., Hoggard, M., Cowton, L., and White, N.: Reassessing the thermal structure of oceanic lithosphere with revised global inventories  
of basement depths and heat flow measurements, *Journal of Geophysical Research: Solid Earth*, 123, 9136–9161, 2018.
- 680 Samuel, H.: A deformable particle-in-cell method for advective transport in geodynamic modelling, *Geophysical Journal International*, 214,  
1744–1773, 2018.



- Schierjott, J. C., Thielmann, M., Rozel, A. B., Golabek, G. J., and Gerya, T. V.: Can grain size reduction initiate transform faults? Insights from a 3-D numerical study, *Tectonics*, 39, e2019TC005 793, 2020.
- Schmid, D. W. and Podladchikov, Y. Y.: Analytical solutions for deformable elliptical inclusions in general shear, *Geophysical Journal International*, 155, 269–288, 2003.
- Schubert, G., Turcotte, D. L., and Olson, P.: *Mantle Convection in the Earth and Planets, Part 1*, Cambridge, 2001.
- Sime, N., Maljaars, J. M., Wilson, C. R., and van Keken, P. E.: An exactly mass conserving and pointwise divergence free velocity method: Application to compositional buoyancy driven flow problems in geodynamics, *Geochemistry, Geophysics, Geosystems*, 22, e2020GC009 349, 2021.
- 685 Sime, N., Wilson, C. R., and van Keken, P. E.: A pointwise conservative method for thermochemical convection under the compressible anelastic liquid approximation, *Geochemistry, Geophysics, Geosystems*, 23, e2021GC009 922, 2022.
- Stein, C. A. and Stein, S.: A model for the global variation in oceanic depth and heat flow with lithospheric age, *Nature*, 359, 123–129, 1992.
- Strauss, W. A.: *Partial differential equations: An introduction*, John Wiley & Sons, 2007.
- Tackley, P. J. and King, S. D.: Testing the tracer ratio method for modeling active compositional fields in mantle convection simulations, *695 Geoch. Geoph. Geosystems*, 4, 2001GC000 214/1–15, 2003.
- Thielmann, M., May, D. A., and Kaus, B. J. P.: Discretization Errors in the Hybrid Finite Element Particle-in-cell Method, *Pure and Applied Geophysics*, 171, 2165–2184, 2014.
- Trim, S. J., Butler, S. L., McAdam, S. S., and Spiteri, R. J.: Manufacturing an exact solution for 2D thermochemical mantle convection models, *Geochemistry, Geophysics, Geosystems*, 24, e2022GC010 807, 2023a.
- 700 Trim, S. J., Butler, S. L., and Spiteri, R. J.: The impact of velocity update frequency on time accuracy for mantle convection particle methods, *Authorea Preprints*, 2023b.
- van Keken, P., King, S., Schmeling, H., Christensen, U., Neumeister, D., and Doin, M.-P.: A comparison of methods for the modeling of thermochemical convection, *Journal of Geophysical Research: Solid Earth*, 102, 22 477–22 495, 1997.
- Van Zelst, I., Wollherr, S., Gabriel, A.-A., Madden, E. H., and van Dinther, Y.: Modeling megathrust earthquakes across scales: One-way coupling from geodynamics and seismic cycles to dynamic rupture, *Journal of Geophysical Research: Solid Earth*, 124, 11 414–11 446, 705 2019.
- Wang, H., Agrusta, R., and van Hunen, J.: Advantages of a conservative velocity interpolation (CVI) scheme for particle-in-cell methods with application in geodynamic modeling, *Geochemistry, Geophysics, Geosystems*, 16, <https://doi.org/10.1002/2015GC005824>, 2015.
- Zhong, S.: Analytic solutions for Stokes' flow with lateral variations in viscosity, *Geophysical Journal International*, 124, 18–28, 1996.
- 710 Zhong, S., McNamara, A., Tan, E., Moresi, L., and Gurnis, M.: A benchmark study on mantle convection in a 3-D spherical shell using CitcomS, *Geochem. Geophys. Geosyst.*, 9, Q10 017, 2008.